VORTEX DYNAMICS OF VERTICAL-AXIS WIND TURBINES ON MARS ECCOMAS CONGRESS 2024

Harry J. Dunn[1*]**, Mohsen Lahooti**[1]**, Nilanjan Chakraborty**[1]**, Ankang Gao** [2]

[1] School of Engineering, Newcastle University, Newcastle-Upon-Tyne NE1 7RU, UK

[2] Department of Modern Mechanics, University of Science and Technology of China, China

* h.dunn1@newcastle.ac.uk

Key words: Computational Fluid Dynamics, DNS , spectral/ hp element method, Vortex Dynamics, VAWT

Summary. Simulation of vertical-axis wind turbines (VAWT) is challenging due to the high-speed rotation of the blades, complex high-Reynolds number turbulent flow with massive separation involved. Addressing such problems requires an efficient numerical approach to robustly handle the dynamics of the geometry while accurately predicting the flow dynamics. DNS simulations have been conducted for the first time to the best of the authors knowledge on a VAWT. This was achieved by using a framework incorporating a moving reference frame formulation (MRF) of Navier-Stokes (NS) equations with the spectral/ hp method within the Nektar++ framework. DNS was performed upon a quasi-$3D$ (homogeneous extrusion of the $2D$ model in the 3rd dimension), three-bladed, straight-bladed Darrieus VAWT. The environmental conditions were akin to the low pressure, low Reynolds number atmosphere found on Mars allowing for this work to be extended to assessing VAWTs potential as an energy source on extra-terrestrial missions, connecting high-order methods to industrial applications. The effect of the order of the polynomial expansion of the variables as well as the resolution within the extrusion upon the present vortex dynamics and aerodynamic forces has been assessed.

1 INTRODUCTION

With the advance of space exploration and the prospect of interstellar habitation off planets such as Mars in the near future, the discussion surrounding the energy sources for these colonies has grown ever more important. Whilst solar and nuclear power generation form the majority of the discussion [1], the former will be impacted by the frequent, intense dust storms that occur on Mars [2], and the latter is less suitable for early colonies due to the complexity of manufacture, transportation and installation, along with the high risk in the case of failure [1]. By incorporating wind energy into a hybrid-source energy system, the risk of dust storms upon energy resources is alleviated whilst allowing for other sources to be integrated when suitable.

In parallel, On Earth, large-scale wind energy is produced by horizontal-axis wind turbines (HAWT) at industrial scale rather than VAWT due to their higher efficiency compared to VAWTs. However, VAWT's ease of installation, manufacture and maintenance make it suitable for isolated, hard-to-reach locations [3], resulting in an interesting alternative for early

Martian colonies where supplies will be limited and infrequently delivered. These advantages also partially underlie predictions for VAWT use within floating offshore wind farms in the foreseeable future, along with their lower centre-of-gravity and negligible gravitational cyclic loading [3, 4, 5], with a major trend within the wind energy industry being these floating platforms.

The complex vortex dynamics governing VAWT performance, such as dynamic stall and blade-wake interactions, require high-fidelity computational approaches to accurately predict them [6, 7, 8]. Here, a novel moving reference frame (MRF) approach within the spectral/ hp element framework Nektar++ [9] is applied to conduct DNS to investigate VAWT aerodynamics within the low Reynolds number (Re) Martian atmosphere, marking the first time DNS has been performed for VAWT. Despite the potential for VAWTs for Martian application, research on their performance in low Re conditions is scarce.

To date, only one study has directly addressed VAWT performance on Mars, conducting an optimisation study utilising RANS to predict laminar to turbulent transition and the Double-Multiple Streamtube model to predict aerodynamic loads [2]. Both of these approaches are low-fidelity and thus overlook the inherently complex flow dynamics involved. More generally, RANS approaches are the most common approach to simulating VAWT. The low computational cost allows for the simulation of full or multiple turbines at higher Re as is typically found on Earth, whilst maintaining reasonable power predictions [10]. RANS, however, is unable to predict laminar-to-turbulent transition, massively separated flows and tends not to extend well to complex geometries as its model parameters is based on canonical turbulent flows. [11, 12, 13]. Using LES addresses many of these issues, seeing greater resolution of the flow dynamics and increased alignment with experimental results with regards to aerodynamic performance [6, 7, 8, 10]. The main disadvantage of LES stems from its sensitivity to subgrid-scale model influencing the prediction of unsteady, turbulent flow phenomena [14]. By further increasing the resolution by performing DNS, it is hoped to overcome these challenges, offering previously uncaptured vortex dynamics.

As DNS simulations for VAWT constitute a novel area of research, it is necessary to conduct preliminary studies to establish a robust computational framework. This study also aims to offer insights VAWT vortex dynamics at low Re numbers, an area often neglected in favor of Earth-typical higher Re conditions which range from $\mathcal{O}\left(10^6\right)$ to $\mathcal{O}\left(10^8\right)$.

2 PROBLEM DESCRIPTION AND NUMERICAL METHODOLOGY

The three-bladed, straight-bladed Darrieus VAWT used in this investigation is based upon the specifications typically used within small-medium scale VAWT [16] and is shown in Figure 1. The aerofoils are modelled as ellipses with a maximum thickness of $0.18c$. Approximating the aerofoils as ellipses facilitated more streamlined mesh generation, making them suitable for preliminary stage studies. Although the ellipses deviate from typically used aerofoils, they are expected to provide valuable insights. These insights will be applicable to future NACA series simulations, where the effects of these geometrical differences will also be analysed. These ellipses have a chord length $c = 0.3m$, with the turbine having a radius, $R = 1m$ and the central shaft having a radius $R_s = 0.1m$. A homogenous extrusion in the z-direction is performed, resulting in periodic boundaries at the aerofoil's spanwise boundaries. The extrusion, and therefore the aerofoils, have a span $L_z = 0.2c$, with this being a common choice in NACA aerofoil investigations [17]. The resolution of this extrusion is determined by the number of Fourier modes, N_z, populating the

extrusion, with the impact of N_z a primary focus of the study. The VAWT is encapsulated within an MRF zone where all surfaces are defined as non-slip walls (background is discussed further below). The MRF zone has a translational speed of $u = 1m/s$, $v, w = 0m/s$ in the x, y, and z directions respectively, resulting in a free-stream velocity $U_\infty = -1m/s$. An angular velocity of $\Omega = 15rad/s$ anti-clockwise is additionally applied to the MRF. Environmental conditions akin to Mars [2] resulted in $Re = 4,500$ with this being calculated from $\Omega R = 15m/s$ and c as seen in Equation 1 where ν is the kinematic viscosity.

$$Re \;\; = \;\; \frac{\Omega R \cdot c}{\nu} \tag{1}$$

The radius of the far-field boundary, $R_o = 500R$, has been set to a high value to limit any possible interactions with the VAWT wake. Throughout this far-field, a convective boundary is applied in accordance with [18]. The physical simulation time $t = 6.28s$ corresponds to 15 rotations, with a timestep $\Delta t = 5 \times 10^{-6}s$ with Spectral Vanishing Viscosity (SVV) used at the sub-grid level.

The spectral/ hp element method within the Nektar++ framework was used to investigate the problem set-up described above. Nektar++ is an open-source, C++, framework with excellent High Performance Computing (HPC) scalability [9]. Within spectral/ hp element method the domain is discretised into a tessellation of elements of arbitrary size, with each element then expanded with a polynomial of arbitrary order $\mathcal{P}$. The spectral/hp element method therefore enjoys the geometric flexibility present within classical low-order finite element methods and the exponential convergence properties of spectral methods. With regards to fluid dynamics applications, spectral/ hp element method is characterised by low numerical diffusion and dispersion suitable for high-fidelity DNS simulations of turbulent flows. Nektar++ can accommodate the complex geometries of VAWT with a range of supported unstructured high-order element types, specifically with tetrahedra, prisms, pyramids, and hexahedra. Additionally, Nektar++ contains several numerical techniques such as SVV, Gradient Jump Penalisation (GJP), and dealiasing.

As discussed in Section 1, the simulation of VAWT is challenging due to the high-speed rotation of the blades and complex high-Re number turbulent flow with massive separation involved. Whilst the present research focusses upon the lower range of Re, an efficient numerical approach to robustly handle the dynamics of the geometry while accurately predicting the flow dynamics is required as we look to extend the study towards higher Re. To address such requirements, a moving reference frame (MRF) of the NS equations within the incompressible Navier-Stokes (NS) solver of the Nektar++ framework [15] is used. The MRF method is based on the absolute velocity formulations in a non-inertial frame, providing further robustness and stability for numerical simulation [19]. The governing equations in the MRF frame is summarised in Equation 2-3 where $\mathbf{u}$ and p are the flow velocities and pressures in the absolute frame respectively, $\mathbf{u}_0$ and $\boldsymbol{\omega}_0$ are the MRF linear and angular velocities in the stationary frame, $\mathbf{x}$ is the is the position vector in moving reference frame from the centre of rotation, $\mathbf{f}$ is the forcing term, and ρ and ν are the density and kinematic viscosity respectively.

$$\frac{\partial \mathbf{u}}{\partial t} + (\mathbf{u} - \mathbf{u}_0 - \boldsymbol{\omega}_0 \times \mathbf{x}) \cdot \nabla \mathbf{u} + \boldsymbol{\omega}_0 \times \mathbf{u} \;\; = \;\; -\frac{1}{\rho}\nabla p + \nu \nabla^2 \mathbf{u} + \mathbf{f} \tag{2}$$

$$\nabla \cdot \mathbf{u} \;\; = \;\; 0 \tag{3}$$
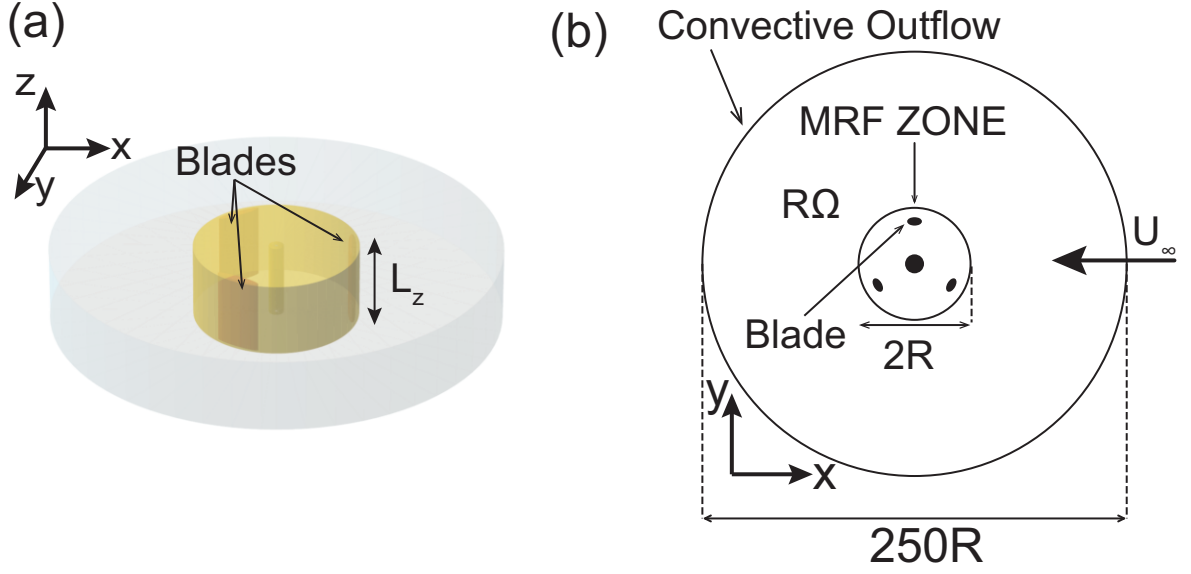
Figure 1: Schematic for VAWT used in numerical simulation (a) 3D view (b) top view
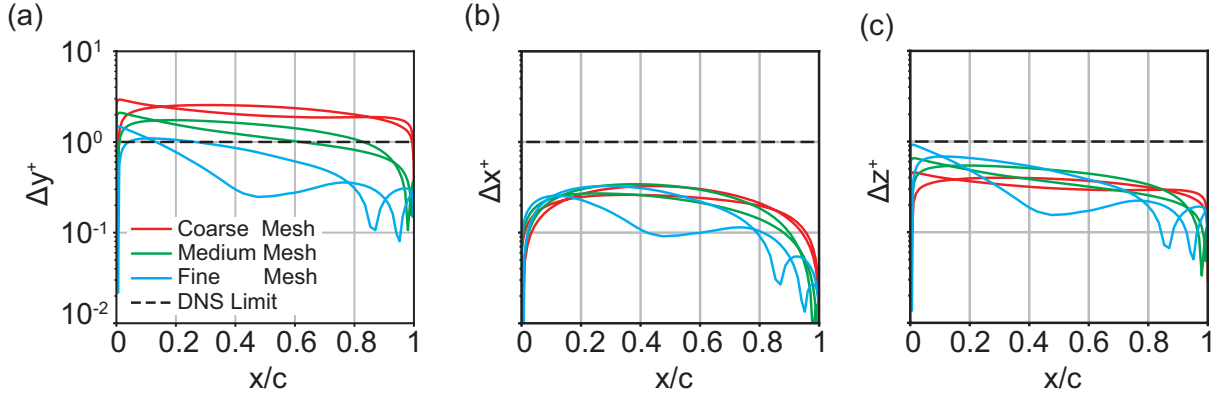

Figure 2: Dimensionless wall distances, a) Δy^+, b) Δx^+, c) Δz^+, at the aerofoil

2.1 Grid Resolution

Initially, a grid resolution study is conducted for $\mathcal{P} = 3$ and $N_z = 16$ to ensure suitable refinement in the macro-mesh. Figure 2 shows the dimensionless wall distances at the aerofoil in the normal, streamwise and spanwise directions, denoted by $\Delta y^+, \Delta x^+, \Delta z^+$ respectively. As evident from Figure 2, all these distances are less than 1, falling within the DNS requirements. As the DNS requirements for Δz^+ are less stringent than for Δx^+ and Δy^+, this indicates that the current number of Fourier planes may be unnecessary, with this being explored further within Section 2.3. The final, DNS-resolved macro-mesh is shown with Figure 3
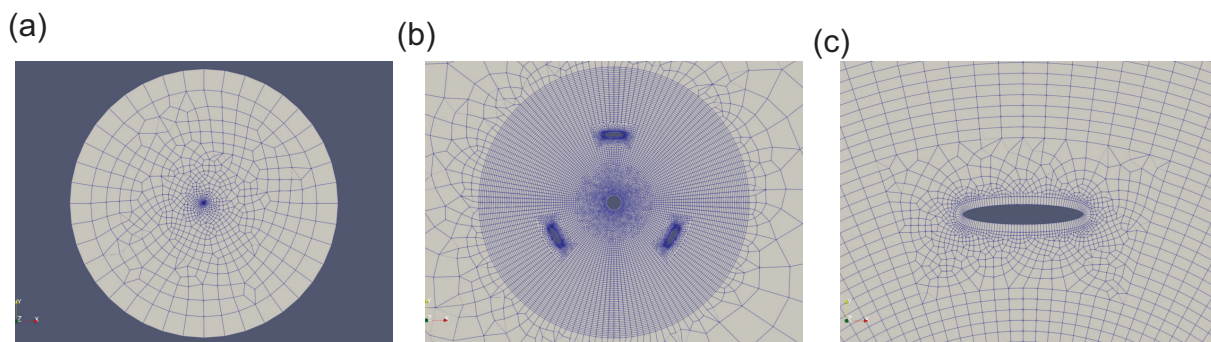
4

(a)

(b)

(c)

Figure 3: Mesh prior to polynomial expansion of the base variables a) far-field b) near-field c) close to the aerofoil

2.2 Effect of Polynomial Order

Previously $\mathcal{P} = 3$ looked suitable when ensuring refinement within the macro-mesh. However, upon observing its capabilities at resolving the flow dynamics it is clear higher $\mathcal{P}$ is required. Figure 4 depicts that $\mathcal{P} = 3$ is only sufficient in capturing the largest flow features, and does not resolve the wake (Figure 4a). Increasing to $\mathcal{P} = 4$ offers noticeable improvement at capturing velocity gradients, particularly along the trailing edges, as well as capturing additional complexities within the near-wake of each aerofoil and smaller-scale vortices (Figure 4b). These improvements are expanded upon as $\mathcal{P}$ is increased to 5 and 6. More detail is captured regarding the vortex shedding mechanisms and the flow features about the VAWTs circumference (Figure 4c-4d). Increasing $\mathcal{P}$ from $\mathcal{P} = 5$ to $\mathcal{P} = 6$ still captures further detail, particularly regarding the resolution of smaller-scale structures. Furthermore, $\mathcal{P} = 6$ resolves more complex flow dynamics within the wake, as seen by the more sharply defined patterns of alternating polarity for the normalised x-component of velocity u^* (only x-component discussed here due to strong similarities with the y-component). These wake structures are crucial as they underlie the blade-wake interactions. Despite increasing $\mathcal{P}$ therefore progressively resolves finer scales, these smaller structures only yield diminishing effects on the overall flow while resolving them leads to additional computational costs. Therefore, investigation of higher $\mathcal{P}$ has been deferred to future work due to resource allocation prioritisation.

A close-up to the aerofoil is highlighted in Figure 5 to assess whether the resolution differences between $\mathcal{P} = 5$ and $\mathcal{P} = 6$ derive from the boundary layer resolution. The most striking observation is the difference in the extent of flow separation between these two polynomial orders. For $\mathcal{P} = 5$, flow separation occurs over much more of c and deeper into the VAWTs inner region (for $R < 1$). In contrast, $\mathcal{P} = 6$ captures the separation bubble with more definitive separation/ reattachment, highlighting improved capability with handling separated flow. Focussing upon the upper region of the aerofoil, $\mathcal{P} = 6$ once again captures more detail, highlighted by the velocity gradients at approximately 80% of c. In the near wake, $\mathcal{P} = 6$ also resolves sharper patterns of vortices of alternating polarity.

Similar to the velocity contours, Figure 6 shows a general increase in resolution of the normalised z-component of vorticity, ω^*, as $\mathcal{P}$ increases from 3 to 6. When the aerofoils undergo large fluctuations in angle of attack past their critical stall angle, dynamic stall can occur. Within dynamic stall, unsteady vortices propagate from the leading edge, being shed from the
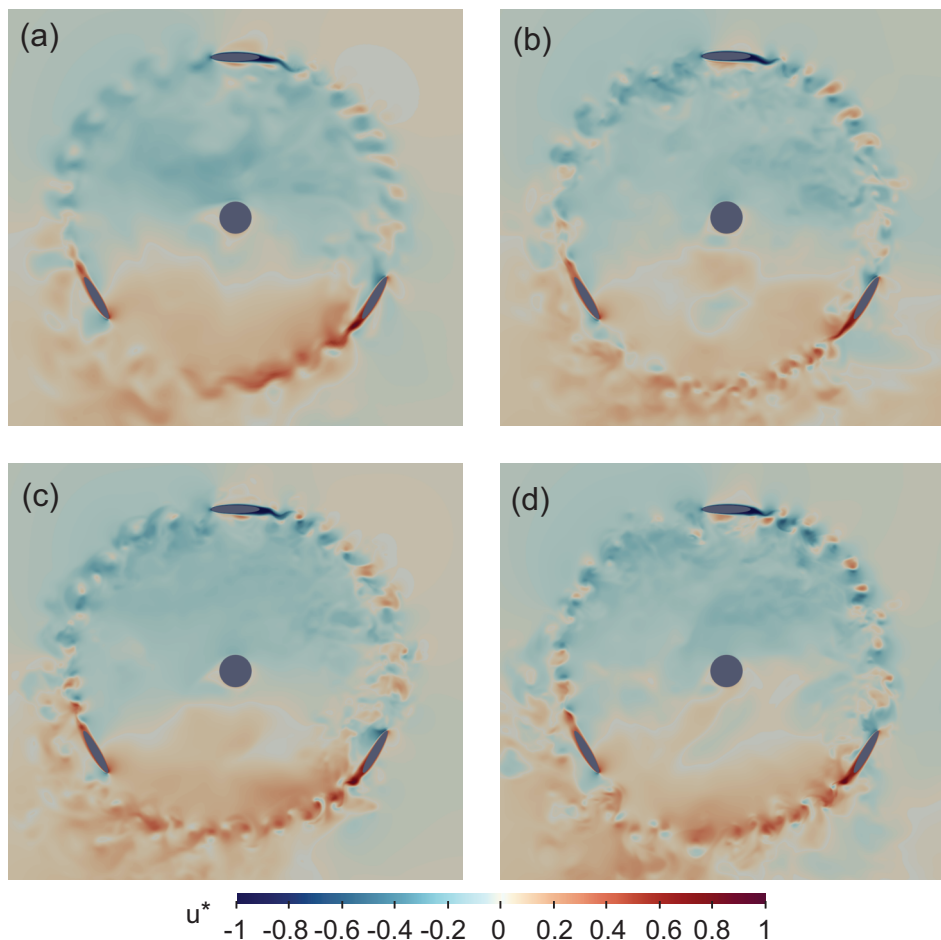
Figure 4: Comparison of the instantaneous normalised x-component of velocity, $u^* = u/\Omega R$, for a) $\mathcal{P} = 3$, b) $\mathcal{P} = 4$, c) $\mathcal{P} = 5$, d) $\mathcal{P} = 6$

trailing edge. Additional blade interactions with the free-stream flow results in further vortex shedding. These vortices are then either convected downstream, or propagate about the rotational path of the aerofoils. Due to the low $U_\infty = 1m/s$ in comparison to the blade-tip speed, $\Omega R = 15m/s$, the amount of downstream vorticity convection is low in comparison to those about the rotational path. The high tip-speed-ratio, $\Omega R/U_\infty$, therefore explains why the vast majority of vortex structures are located around the VAWTs circumference (Figure 6).

Increasing $\mathcal{P}$ leads to better resolution of the vortex shedding during dynamic stall, which results in patterns of vortex structures of alternating polarity stemming from the aerofoils trailing edges. This effect is most clearly seen for the top blade within Figure 6a-6d, with these patterns having improved clarity throughout the VAWTs circumference for $\mathcal{P} = 6$. In contrast, for $\mathcal{P} = 3$, this pattern is barely visible, filtering out the vast majority of these structures. Also noteworthy is the increase in complexity of the patterns of the shed vortices as $\mathcal{P}$ increases. This is most clearly highlighted for the top blade within Figure 6a-6d, where the ω^* structures are much sharper in the wake immediately following the trailing edge for $\mathcal{P} = 5, 6$ compared to $\mathcal{P} = 3, 4$. Similarly to u^*, the smallest-scale vortices are only present for $\mathcal{P} = 6$, with lower $\mathcal{P}$ values

6

(a)
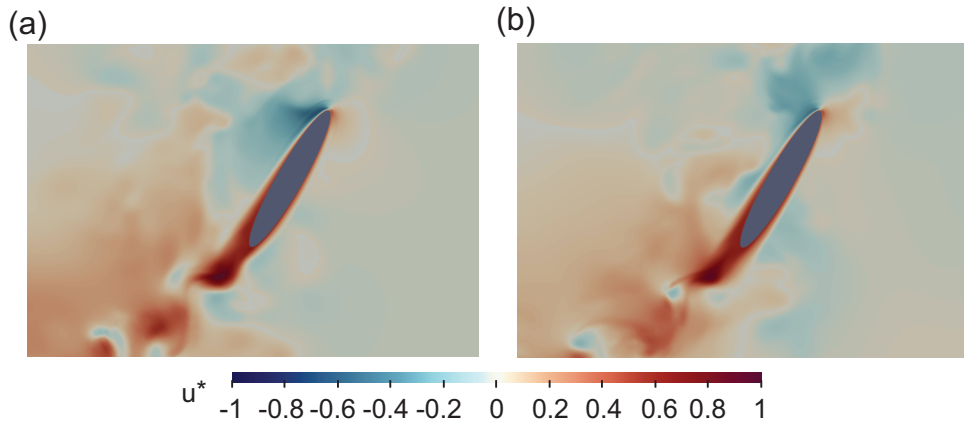
(b)

u* -1 -0.8 -0.6 -0.4 -0.2 0 0.2 0.4 0.6 0.8 1

Figure 5: Comparison of the instantaneous normalised x-component of velocity, $u^* = u/\Omega R$, for varying polynomial order close to the airfoil.
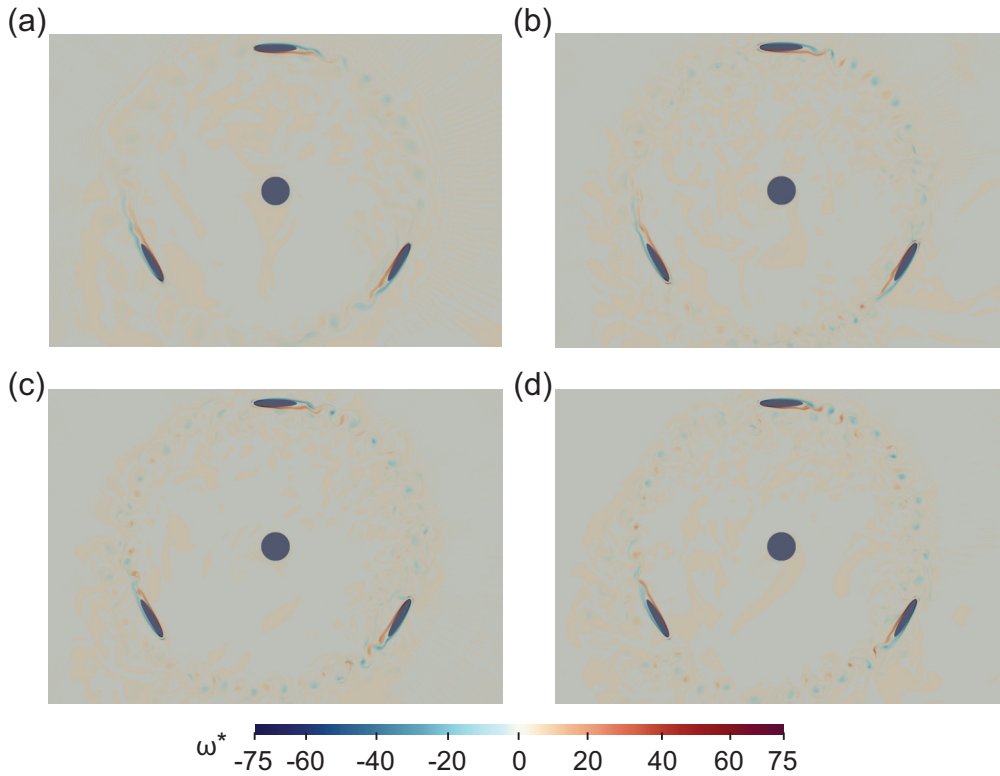
offering only a more dissipative solution.

(a)

(b)

(c)

(d)

ω* -75 -60 -40 -20 0 20 40 60 75

Figure 6: Comparison of the instantaneous normalised z-component of vorticity, $\omega^* = \omega(c/\Omega R)$, for a) $\mathcal{P} = 3$, b) $\mathcal{P} = 4$, c) $\mathcal{P} = 5$, d) $\mathcal{P} = 6$

As $\mathcal{P}$ increases from 3 to 6, increased detail within the Q-criterion is captured (Figure 7). This is highlighted by the larger turbulent structures seen within $\mathcal{P} = 3$ (Figure 7a) compared

to higher $\mathcal{P}$ values. Increasing to $\mathcal{P} = 4, 5$ allows for increased resolution, particularly close to the aerofoils and along the wake region (bottom right of Figure 7b-Figure 7c), resolving further blade-wake interactions. Increasing to $\mathcal{P} = 6$ still offers improvements with capturing smaller-scale structures but particularly with regards to the patterns of these turbulent structures. Whilst these patterns also become clearer as $\mathcal{P}$ is increased from 3 to 5, at $\mathcal{P} = 6$ interconnected chains of vortices extend further downstream towards the bottom right than what is seen at lower $\mathcal{P}$ (Figure 7d). Interestingly, $\mathcal{P} = 6$ also better captures the impact of the turbines rotation upon the wake, with the bottom right region having a larger rotational component which is not captured as accurately at lower $\mathcal{P}$.

The inner region is also sensitive to $\mathcal{P}$, with $\mathcal{P} = 3$ filtering out vast amounts of turbulent structures that are identified by $\mathcal{P} = 4$. Surprisingly, increasing $\mathcal{P}$ from 4 to 5 reduces the amount of turbulent structures present, perhaps due to the instantaneous nature of Figure 7. To further investigate this, using a suitable time-averaging technique is planned for future work. The filtering seen from $\mathcal{P} = 4$ to $\mathcal{P} = 5$ is not seen as $\mathcal{P}$ is increased to 6, with this polynomial order offering the most comprehensive insights into the turbulent structures.

Overall, for Q-criterion, increasing to $\mathcal{P} = 6$ still offers benefits in comparison to lower $\mathcal{P}$, in which the predictions are more dissipated. As mentioned before, increasing $\mathcal{P}$ further will resolve more of the energy cascade process, however, the impact on the overall flow will reduce with computational costs increasing. Hence, this aspect has been postponed due to resource allocation prioritisation. It is also worthwhile to note that the small $L_z = 0.2c$, utilised at present will limit the possibility of identifying low-frequency, spanwise vortices, although these are predicted to a minimal impact on the overall flow dynamics. Future quasi-3D simulations with greater L_z lengths and full 3D simulations, will address this limitation, investigating the presence and impact of these vortices, if they exist.

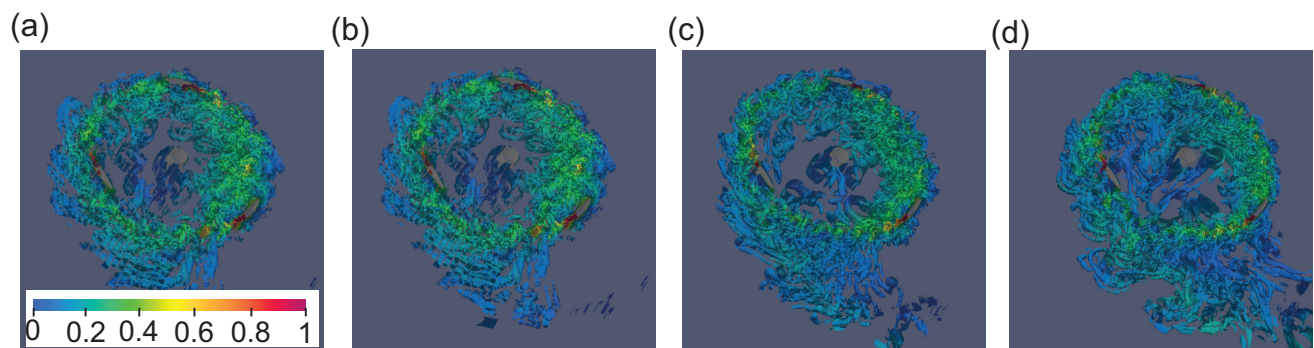Figure 7: Instantaneous isosurfaces for Q-criterion = 15 for a) $\mathcal{P} = 3$, b) $\mathcal{P} = 4$, c) $\mathcal{P} = 5$, d) $\mathcal{P} = 6$. Coloured with the velocity magnitude.

The predicted forces for $\mathcal{P} = 4$ has a clear offset from those for $\mathcal{P} = 5, 6$ (Figures 8a-8b), resulting in a substantial difference within the calculated moment (Figures 8c). The difference, however, between the forces for $\mathcal{P} = 5$ and $\mathcal{P} = 6$ are relatively small, with strong alignment in the prediction for the majority of the rotation period. This aligns with the earlier observation that increasing P resolves smaller-scale structures, but these have a decreasing effect on the overall flow. Due to only having these small differences in the F_x^* and F_y^* over the majority of the rotation period, it can be concluded that $\mathcal{P} = 6$ is likely a good choice for simulations,

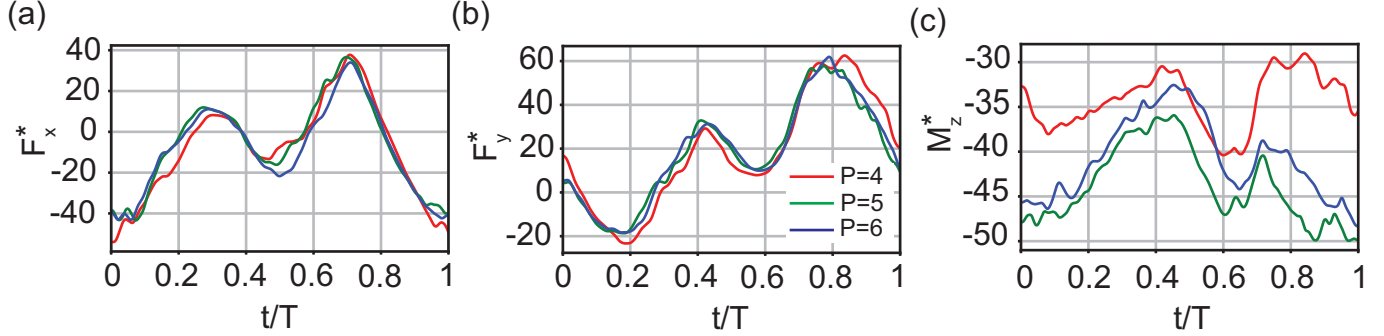and further increases in P would not substantially contribute to the flow and aerodynamic force predictions.

Figure 8: Comparison of (a) normalised x-component of force $F_x^* = F_x/0.5\rho U_\infty^2 c$, (b) normalised y-component of force $F_y^* = F_y/0.5\rho U_\infty^2 c$, and (c) normalised z-component of moment $M_Z^* = M_Z/0.5\rho U_\infty^3 c$ over one rotation period (t/T) for varying polynomial orders

The above investigation into the effect of $\mathcal{P}$ upon VAWT flow dynamics has highlighted it is crucial to accurately determining VAWT flow dynamics. Consistently, $\mathcal{P} = 6$ gives the least dissipative solution seeing improvements its ability to identify flow separation, vortex shedding, blade-wake interactions and resolving smaller-scale structures. The force predictions convey the diminishing overall effect on the flow dynamics that these additionally resolved flow features for higher $\mathcal{P}$. It is worthwhile to note these results are instantaneous, and hence time-averaging is valuable consideration to unravel which flow features are steady over each rotation.

2.3 Resolution in the Homogenous Direction

This section investigates the impact N_z has within the homogenous extrusion whilst $\mathcal{P} = 6$ is held constant. Within the u^* contours, smaller-scale structures are resolved and the patterns of alternating polarity are more sharply defined, with this being best observed following the top aerofoils trailing edge (Figures 9a-9c). Additionally, the inner region is largely uniform in each hemisphere for $N_z = 8$, with the top and bottom hemispheres being largely negative and positive respectively (Figure 9a). This uniformity is continually reduced as N_z is increased with more velocity gradients, likely a by-product of the VAWTs rotation, observed in each hemisphere (Figures 9b-9c).

Close to the aerofoil, $N_z = 8$ predicts massive flow separation across the aerofoil's chord (Figure 10a). Increasing the resolution in the homogenous direction reveals a separation bubble (Figures 10b-10c). The separation bubble then decreases in size and moves closer to the aerofoils leading edge from $N_z = 16$ to $N_z = 32$. The aerofoils wake structure is additionally impacted, with higher N_z capturing more gradual velocity gradients in the wake direction. Interestingly, $N_z = 16$ captures an eddy within its wake which is not seen for $N_z = 32$, with this to be analysed further with time-averaging to ascertain its significance.

Figures 11a-11c show that increasing N_z introduces similar effects for ω^* as increasing $\mathcal{P}$ did (Section 2.2). As N_z increases from 8 to 32, the wake tends to be better resolved, as observed by the sharper patterns of ω^* of alternating polarity. The complexity of these patterns also
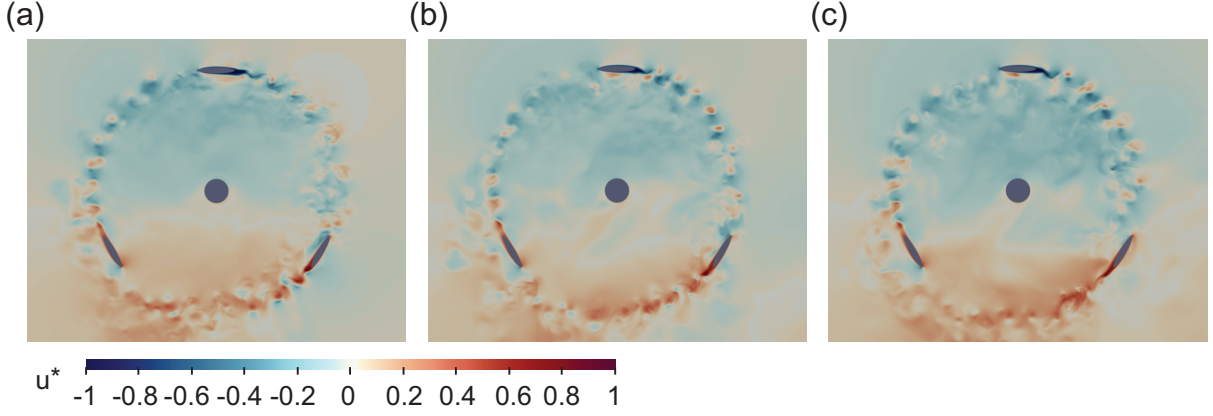
(a) (b) (c)

Figure 9: Comparison of the instantaneous normalised x-component of velocity, $u^* = u/\Omega R$, for a) $N_z = 8$, b) $N_z = 16$, c) $N_z = 32$
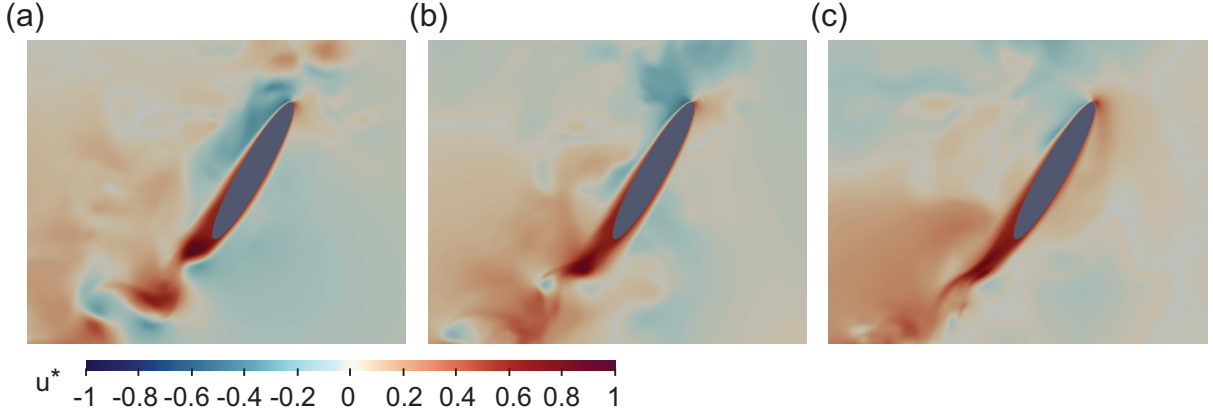
(a) (b) (c)

Figure 10: Comparison of the instantaneous normalised x-component of velocity, $u^* = u/\Omega R$, for a) $N_z = 8$, b) $N_z = 16$, c) $N_z = 32$

increases with higher N_z, containing smaller eddies.

Increasing the resolution in the homogenous direction has led to similar outcome to those seen when increasing $\mathcal{P}$, with finer flow structures predicted, as well as better capturing the VAWT rotation effects upon the flow field, with this largely concerning the inner region. Once again, the instantaneous nature of the results may have had some impact on this, with time-averaging planned to investigate this further.

3 CONCLUSION

VAWT flow dynamics in low Re show strong sensitivity to both $\mathcal{P}$ and N_z, with the increased resolution giving more accurate predictions for smaller-scale turbulent and vortex structures, flow separation, wake structures, and blade-wake interactions. At higher $\mathcal{P}$ and N_z values, the impact on flow dynamics diminishes, as only minimal impact, smaller-scale structures are additionally resolved. It is evident from Figure 8, that $\mathcal{P} = 6$ is a good compromise between capturing important flow features whilst minimising computational cost. For N_z massive differences are
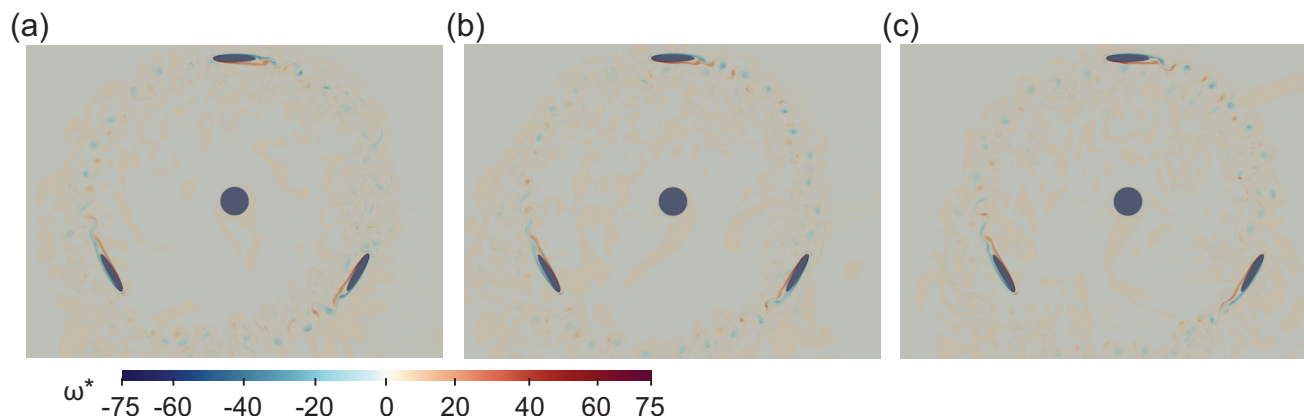
(a) (b) (c)

Figure 11: Comparison of the instantaneous normalised z-component of vorticity, $\omega^* = \omega(c/\Omega R)$, a) $N_z = 8$, b) $N_z = 16$, c) $N_z = 32$

seen between $N_z = 8$ and $N_z = 16, 32$, highlighted by the formers inability to resolve the separation bubble instead predicting massive flow separation. For $N_z = 32$, this separation bubble had yet more clarity. These findings provide a good foundation to begin investigations on the aerofoils at higher Re in more computationally demanding cases. Future work additionally aims to 1) address any potentially hidden low-frequency spanwise vortices through quasi-$3D$ and full $3D$ investigations, although the effects of these are expected to be limited 2) investigate the time-averaged quantities to develop a clear picture of the steady vs unsteady behaviour.

4 ACKNOWLEDGEMENTS

REFERENCES

[1] Hartwick, V. L., O. B. Toon, J. K. Lundquist, O. A. Pierpaoli, and M. A. Kahre. 2023. "Assessment of wind energy resource potential for future human missions to Mars." Nature Astronomy 7, no. 3: 298-308. http://doi.org/10.1038/s41550-022-01851-4

[2] Kumar, V., M. Paraschivoiu, and I. Paraschivoiu. 2010. "Low Reynolds Number Vertical Axis Wind Turbine for Mars." Wind Engineering 34, no. 4: 461-476. http://doi.org/10.1260/0309-524X.3.4.461

[3] Li, Y., S. Yang, F. Feng, and K. Tagawa. 2023. "A review on numerical simulation based on CFD technology of aerodynamic characteristics of straight-bladed vertical axis wind turbines." Energy Reports 9: 4360-4379. http://doi.org/10.1016/j.egyr.2023.03.082

[4] Hand, B., and A. Cashman. 2020. "A review on the historical development of the lift-type vertical axis wind turbine: From onshore to offshore floating application." Sustainable Energy Technologies and Assessments 38: 100646. http://doi.org/10.1016/j.seta.2020.100646

[5] Arredondo-Galeana, A., and F. Brennan. 2021. "Floating Offshore Vertical Axis Wind Turbines: Opportunities, Challenges and Way Forward." Energies 14, no. 23: 8000. http://doi.org/10.3390/en14238000

[6] Li, C., S. Zhu, Y. Xu, and Y. Xiao. 2013. "2.5D large eddy simulation of vertical axis wind turbine in consideration of high angle of attack flow." Renewable Energy 51: 317-330. http://doi.org/10.1016/j.renene.2012.09.011

[7] Sheidani, A., S. Salavatidezfouli, G. Stabile, and G. Rozza. 2023. "Assessment of URANS and LES methods in predicting wake shed behind a vertical axis wind turbine." Journal of Wind Engineering and Industrial Aerodynamics 232: 105285. http://doi.org/10.1016/j.jweia.2022.105285

[8] He, J., X. Jin, S. Xie, L. Cao, Y. Wang, Y. Lin, and N. Wang. 2020. "CFD modeling of varying complexity for aerodynamic analysis of H-vertical axis wind turbines." Renewable Energy 145: 2658-2670. http://doi.org/10.1016/j.renene.2019.07.132

[9] Moxey, D., C. D. Cantwell, Y. Bao, A. Cassinelli, G. Castiglioni, S. Chun, E. Juda, E. Kazemi, K. Lackhove, J. Marcon, G. Mengaldo, D. Serson, M. Turner, H. Xu, J. Peiró, R. M. Kirby, and S. J. Sherwin. 2020. "Nektar++: Enhancing the capability and application of high-fidelity spectral/hp element methods." Computer Physics Communications 249: 107110. http://doi.org/10.1016/j.cpc.2019.107110

[10] Shamsoddin, S., and F. Porté-Agel. 2016. "A Large-Eddy Simulation Study of Vertical Axis Wind Turbine Wakes in the Atmospheric Boundary Layer." Energies 9, no. 5: 366. http://doi.org/10.3390/en9050366

[11] Venkatachari, B., P. Paredes, J. Derlaga, P. Buning, M. Choudhari, F. Li, and C. Chang. 2021. "Assessment of RANS-based Transition Models based on Experimental Data of the Common Research Model with Natural Laminar Flow." In AIAA Scitech 2021 Forum. http://doi.org/10.2514/6.2021-1430

[12] Baranova, T. A., V. L. Zhdanov, D. A. Ivanov, J. I. Smulsky, and V. I. Terekhov. 2018. "RANS and LES analysis of a separation region in front of a backward-facing step." Journal of Physics: Conference Series 980: 012026. http://doi.org/10.1088/1742-6596/980/1/012026

[13] Kassem, A., M. Madbouly, and A. Guaily. 2021. "Comparative Study for Different URANS Models for Capturing Flow Separation Inside a Plane Diffuser." In 2021 3rd Novel Intelligent and Leading Emerging Sciences Conference (NILES), 287-290. http://doi.org/10.1109/NILES53778.2021.9600095

[14] Shamsoddin, S., and F. Porté-Agel. 2014. "Large Eddy Simulation of Vertical Axis Wind Turbine Wakes." Energies 7, no. 2: 890-912. http://doi.org/10.3390/en7020890

[15] Nektar++. 2022. "Incompressible Flow Simulation." https://www.nektar.info/notebooks/tutorials/basics-incns-solver/

[16] Alaimo, A., A. Esposito, A. Messineo, C. Orlando, and D. Tumino. 2015. "3D CFD Analysis of a Vertical Axis Wind Turbine." Energies 8, no. 4: 3013-3033. http://doi.org/10.3390/en8043013

[17] Jones, G., M. Santer, and G. Papadakis. 2018. "Control of low Reynolds number flow around an airfoil using periodic surface morphing: A numerical study." Journal of Fluids and Structures 76: 95-115. http://doi.org/10.1016/j.jfluidstructs.2017.09.009

[18] Dong, S. 2015. "A convective-like energy-stable open boundary condition for simulations of incompressible flows." Journal of Computational Physics 302: 300-328. http://doi.org/10.1016/j.jcp.2015.09.017

[19] Lahooti, M., Y. Bao, D. Scott, R. Palacios, and S. J. Sherwin. 2023. "LES/DNS fluid-structure interaction simulation of non-linear slender structures in Nektar++ framework." Computer Physics Communications 282: 108528. http://doi.org/10.1016/j.cpc.2022.108528